
Article:
Issa, I., Ford, K. orcid.org/0000-0002-1080-6193, Rao, M.R. orcid.org/0000-0002-4109-4176 et al. (1 more author) (2019) A magnetic resonance imaging surface coil transceiver employing a metasurface for 1.5T applications. IEEE Transactions on Medical Imaging. ISSN 0278-0062

https://doi.org/10.1109/TMI.2019.2942194

A Magnetic Resonance Imaging Surface Coil Transceiver Employing a Metasurface for 1.5T Applications

Ismail Issa*, Kenneth Lee Ford†, *Senior Member, IEEE,* Madhwesha Rao‡, and Jim M.Wild‡

***Abstract*—A capacitive impedance metasurface combined with a transceiver coil to improve the radio frequency magnetic field for 1.5T magnetic resonance imaging applications is presented. The novel transceiver provides localized enhancement in magnetic flux density when compared to a transceiver coil alone by incorporating an electrically small metasurface using an inter-digital capacitance approach. Full field simulations employing the metasurface show a significant improvement in magnetic flux density inside a homogeneous dielectric phantom, which is also shown to perform well for a range of depths into the phantom. The concept was experimentally demonstrated through vector network analyzer measurements and images have been taken using a 1.5T MRI scanner. The results show there is a 216% improvement in transmission efficiency, a 133% improvement in receiver signal-to-noise-ratio (SNR), and a 415% improvement in transceiver SNR for a particular transmission power when compared against a surface coil positioned at the same distance from the phantom, where these improvements are the maximum observed during experiments.**

***Keywords*—Magnetic resonance imaging, surface coil, capacitive impedance surface, metasurfaces.**

I. Introduction

Magnetic resonance imaging (MRI) is a technique used primarily in medical applications to produce diagnostic images of the human body [1], and is based on the phenomenon of nuclear magnetic resonance (NMR). Radio frequency (RF) coils are used to excite nuclear spins and detect the signal generated by the precessing nuclei [2]. In thermally polarized NMR the signal to noise ratio (SNR) scales with the strength of the static magnetic flux density, B_0, which improves image quality and enables faster image acquisition. Increasing B_0 linearly increases the resonant frequency (Larmor frequency) of RF precession of the nuclei and can impose further challenges in achieving image quality due to inhomogeneities of the RF magnetic flux density, B_1, in the dielectric sample [1]. An associated problem for high frequency (high static magnetic field) MRI systems is exceeding specific absorption ratio (SAR) regulatory limits due to higher unwanted radiation, and dielectric properties of the human tissue, whilst this problem is less of an issue at the Larmor frequencies associated with lower magnetic field systems e.g. 64MHz at 1.5T [3]. It is partly for these reasons that research is being carried out on alternative methods of improving image quality without the need to increase the static magnetic field. One such method is the use of metamaterials and metasurfaces, which have been used in a range of electromagnetic applications, that have been shown to focus/enhance fields in both near and far field [4], [5]. Consequently, these novel materials are a good candidate for MRI applications. The physical attributes of metamaterials and metasurfaces differ as metamaterials provide bulk properties (permittivity and permeability), whereas metasurfaces have been considered by their impedance and electric/magnetic susceptibilities. A specific advantage of metasurfaces, discussed in this paper, is that they can be used as a matching layer between the RF coil and human body, in a similar way to a dielectric pad [6]. Metamaterials are often used as a lens device to focus fields into the body.

Metamaterials were first introduced as being applicable to MRI through the use of flux guides (Swiss roll) that are physically large structures that allowed RF receive coils to be located away from the body, [7]. Lens techniques have been adopted through the use of capacitively loaded split ring resonators [8]–[10], that provide localised image and SNR enhancement. High impedance surfaces (HIS) have also been employed as in-phase reflective shields to improve field strength at 7T [11]–[13], and also at 1.5T [14], [15]. There has also been significant research into wire media based metamaterials and metasurfaces, initially [16] showed how a metallic endoscope can be used to guide fields to an external receive probe. This research led to further, wire based, metasurfaces that have been used for low (1.5T) and high field (7T) applications [17]–[20]. Despite all of the above innovative approaches, the translation of meta-materials in to routine clinical MRI RF engineering products has yet to be made.

In this paper we demonstrate, using theoretical design, numerical simulations, vector network analyzer (VNA) measurements, and MRI measurement in phantoms, that the RF magnetic flux density (B_1) and SNR can be increased when a capacitive impedance surface (CIS) is placed between a RF loop transceiver coil and a homogeneous phantom for ^1H MRI on a 1.5T system. Here, we demonstrate a non-resonant metasurface as compared to structures that employ resonance through the use of lumped components or other means [10], [17], [20]–[22]. Another key novel aspect of the approach is the demonstration of significant B_1 field spatial modulation and SNR improvement away from the center of the RF coil

*I. Issa is with the Department of Electronic and Electrical Engineering, University of Misurata, Misurata, Libya

†K. L. Ford is with the Department of Electronic and Electrical Engineering, University of Sheffield, Sheffield, UK

‡M. Rao and J. Wild are with the POLARIS group, Department of Infection, Immunity and Cardiovascular Disease, University of Sheffield, Sheffield, UK

which would enhance MRI acquisition capability in certain anatomical surface receive applications.

The paper is organized into four technical sections beginning with Section II which discusses the CIS concept and implementation using an interdigital frequency selective surface. Section III describes the numerical characterization of the proposed system. Section IV demonstrates experimental characterization within a laboratory environment and Section V details the results from measurements on a water phantom with a 1.5T MRI scanner.

II. Capacitive Impedance Surface Concept and Implementation

An important parameter for any MRI system is the SNR and the formulation of this is well understood [23], [24] and can be expressed using (1),

$$SNR \propto f^2 \frac{|sin(\gamma\tau|B_1^+|)(B_1^-)^*|}{\sqrt{P_{abs}}}, \tag{1}$$

where f is the Larmor frequency, γ is the gyromagnetic ratio, τ is the RF pulse duration, and P_{abs} is the power absorbed in the system. The remaining terms, B_1^+ and B_1^-, are defined as complex values in (2) and (3) assuming B_0 is aligned along the z-axis.

$$B_1^+ = \frac{B_x + jB_y}{2} \tag{2}$$

$$B_1^- = \left(\frac{B_x - jB_y}{2}\right)^* \tag{3}$$

The positively rotating B_1^+, created when an RF current at the Larmor frequency is passed through the coil, produces a rotating magnetic field which flips the bulk magnetization corresponding to the flip angle and, as such, is useful as a transmission metric, which is often normalised to the square root of the coil input power. In this work the input power is kept constant when making comparisons with and without our proposed technique. Once the RF signal is switched off the coil receives the signal through Faraday's law of induction which is proportional to the complex conjugate of B_1^- and the ratio of $\frac{B_1^-}{\sqrt{P_{abs}}}$ is useful for characterizing receiver sensitivity.

A. Performance evaluation of idealised capacitive impedance surface

Fig. 1a shows a cross section of a dielectric phantom, mimicking a biological sample, spaced a distance, *s*=5mm, away from a homogeneous CIS, which in turn is spaced a distance, *d*=20mm, away from a RF transceiver loop coil. A study of the impact on the spacing, *d*, was carried out similar to previous work [25], and it was found that this spacing provided maximum improvement. The CIS is assumed to be dominated by capacitance and is given by *Z=R-jX*, where in this section the losses are assumed to be zero (R=0) for the idealised case. The RF coil was chosen to be circular for this study and designed for a trade off between depth of field penetration and receiver sensitivity for a 140mm thick dielectric phantom at 63.8MHz (hydrogen proton Larmor frequency at 1.5T),

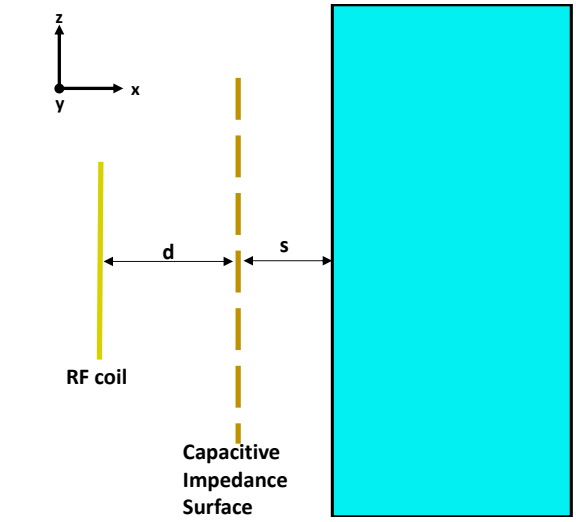

(a) Cross section of proposed concept

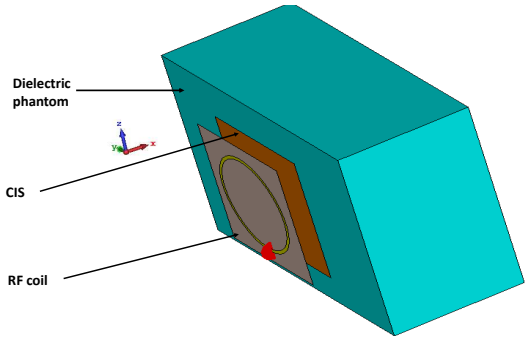

(b) Full field simulation model

Fig. 1: Illustration of capacitive impedance MRI concept

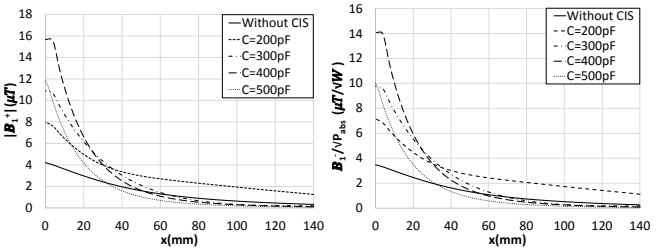

(a) $|B_1^+|$ (b) $|B_1^-|/\sqrt{P_{abs}}$

Fig. 2: Simulations through the centre of a dielectric phantom for a RF loop transceiver employing an ideal CIS, assuming a 1A current source. Note the B_1^+ is normalised to 1W input power.

and resulted in a coil diameter of 12.3cm [1], with a coil width of 6mm. For simulation purposes a whole body homogeneous phantom of length=335mm, width=230mm, thickness=140mm, and $\epsilon_r = 65, \sigma = 0.4S/m, \rho = 1000kg/m^3$ [26], [27] was chosen for comparison with later measurements.

Numerical simulations were performed using the time domain solver within CST Microwave Studio 2015 where the coil was fed with a 1A current source as shown in Fig. 1b and it was assumed that the impedance surface, modelled as a tabulated surface impedance, was 150mmx150mm which has been shown to provide reasonable results in previous studies [15]. The simulation was surrounded by an absorbing boundary condition.

The $|B_1^+|$ and $|B_{1^-}|/\sqrt{P_{abs}}$ along the x-axis, through the coil centre, is shown in Fig. 2 for a range of surface capacitances and is compared to the configuration without CIS. Fig. 2a shows that $|B_1^+|$ can be significantly increased with the use of a CIS with a 4-fold maximum improvement near the surface of the phantom, however, as the capacitance increases further the improvement in $|B_1^+|$ reduces to a point where the surface has a detrimental impact. It is observed that there is a limit in the penetration depth that can be achieved for higher values of capacitance, for instance when the capacitance is 400pF there is no improvement beyond 50mm. Similar trends are observed for $|B_1^-|/\sqrt{P_{abs}}$, shown in Fig. 2b.

B. CIS implementation using an interdigital frequency selective surface

To implement the capacitive impedance a frequency selective surface (FSS) approach was adopted which consists of a periodic array of metallic and dielectric elements. There are a range of options for the geometry of the metallic elements of the FSS, including square patches, Jerusalem crosses, spirals etc. Classic FSS designs tend to have periodic elements which can be a significant fraction of a wavelength which would not be appropriate for MRI at 63.8MHz, as such an interdigital approach was adopted that has been previously reported [15], and has a high capacitance density which provides electrically small unit cell designs. Fig. 3 shows the unit cell of the upper surface of the CIS which has a 0.8mm FR4 substrate (ϵ_r=4.3, $\tan\delta$=0.025) and the lower surface consists of an orthogonal copy of the upper surface to ensure dual polarisation performance, hence the FSS is a two layer design. The inset of Fig. 3 shows the detail of the interdigitation which composes of metallic elements of width w_d, separated by g_d. The capacitance, in pF, of the CIS can be estimated using (4) - (6) [28],

$$C = \frac{\epsilon_{eff} * 10^{-3}(N-1)D}{18\pi}\frac{K(k)}{K'(k)}, \tag{4}$$

where

$$\frac{K(k)}{K'(k)} = \begin{cases} \frac{1}{\pi} ln\left[\frac{2(1+\sqrt{k})}{1-\sqrt{k}}\right] & 0.707 \leq k \leq 1 \\ \frac{\pi}{ln\left[\frac{2(1+\sqrt{k'})}{1-\sqrt{k'}}\right]} & 0 \leq k \leq 0.707 \end{cases} \tag{5}$$

and

$$k = \tan^2\left(\frac{a\pi}{4b}\right), a = w_d/2, b = \frac{w_d + g_d}{2}, k' = \sqrt{1-k^2} \tag{6}$$

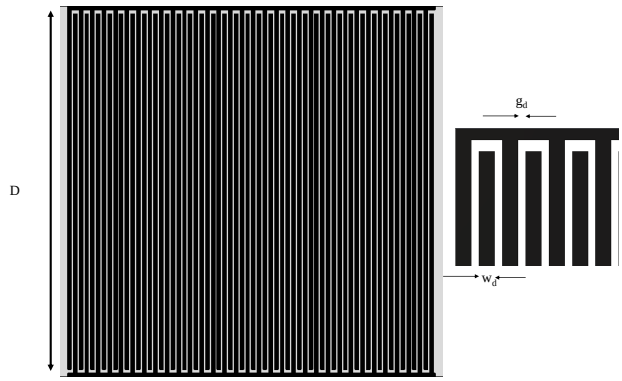

Fig. 3: Front layer of FSS unit cell including interdigitation dimensional details. Note that the black denotes copper.

where $K(k)$ is the complete elliptic integral of the first kind and its complement is $K'(k)$, D is the digit length in mm, N is the number of digits, and $\epsilon_{eff} = \frac{\epsilon_r+1}{2}$. It should be noted that the design equations have uncertainties associated with them, mainly due to the effective permittivity which tends towards $\epsilon_{eff} = \frac{\epsilon_r+1}{2}$ for thick substrates. As the substrate is electrically very thin in this work, in order to reduce losses, these equations are useful as an initial design estimation only and the substrate effect is addressed through full field simulations.

To accurately simulate the FSS properties a full field approach was adopted where the unit cell of the FSS was surrounded by periodic, Floquet mode, boundary conditions which effectively provides an infinite structure that is then illuminated with a plane wave and from this the equivalent impedance of the surface can be easily determined.

In designing the FSS a trade off in the number of unit cells for the total surface area ($150mm \times 150mm$) was considered. It was shown in [10] that the field strength varies inside the phantom due to the periodicity and nulls can be produced between the unit cells. To mitigate against this an odd number of unit cells where the centers of the unit cell and RF coil are aligned is beneficial. Also, to reduce the number of potential nulls in the magnetic field, which would produce field inhomogeneities, a 3 by 3 unit cell arrangement was chosen.

To demonstrate the highest improvement in magnetic field a capacitance of 400pF was chosen for the remainder of this study which led to a unit cell with the following properties (unit cell periodicity P=50mm, D=49mm, N=132, w_d=0.25mm, and g_d=0.12mm). There was also a 0.3mm gap between the ends of the digits and the horizontal metallic strip at the top of the unit cell and there is an inter-unit cell separation of 0.58mm. It was assumed that the metallic elements were $32\mu m$ thick copper.

III. Numerical characterization of FSS implementation

All simulations detailed in this section assume a FSS incorporating nine unit cells with the dimensions resulting from Section II-B.

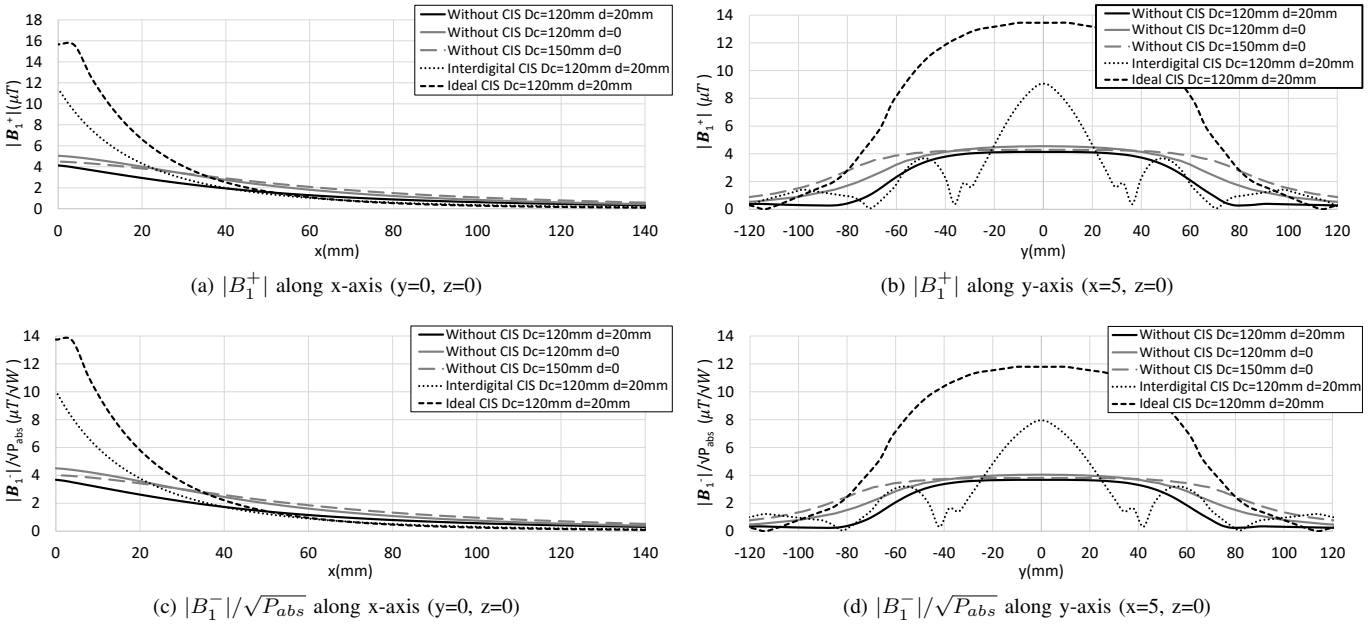

(a) $|B_1^+|$ along x-axis (y=0, z=0)

(b) $|B_1^+|$ along y-axis (x=5, z=0)

(c) $|B_1^-|/\sqrt{P_{abs}}$ along x-axis (y=0, z=0)

(d) $|B_1^-|/\sqrt{P_{abs}}$ along y-axis (x=5, z=0)

Fig. 4: Comparison of simulated performance for ideal CIS, interdigital CIS, and without CIS

A. *Analysis of transceiver performance*

Simulations were carried out with and without the CIS where $|B_1^+|$ and $|B_1^-|/\sqrt{P_{abs}}$ inside the dielectric phantom were monitored along the x-axis and y-axis when fed by a sinusoidal 1A current source. Three 'coil only' scenarios were compared against the 'coil and CIS' scenario. The first is where the coil (diameter $D_c = 120mm$) is placed a distance *d+s=25mm* away from the phantom. This provides a baseline comparison against a fixed coil spacing. The second is where the coil (diameter $D_c = 120mm$), is placed a distance *s=5mm* away from the phantom and provides a more application specific comparison. The third is where the coil (diameter $D_c = 150mm$) is placed a distance *s=5mm* from the phantom, where the coil is the same size as the CIS. We also include an ideal (lossless) CIS for a comparison of what is fundamentally possible. Fig. 4a and Fig. 4b show $|B_1^+|$ along the x-axis and y-axis respectively whilst Fig. 4c and Fig. 4d show $|B_1^-|/\sqrt{P_{abs}}$ simulations.

It can be seen in Fig. 4a and Fig. 4d that, when compared to the coil only ($D_c = 120mm, d = 20mm$), the ideal CIS provides significant improvement near the surface of the phantom and the improvement remains to a depth of 50mm. For the interdigital CIS which includes both copper and substrate losses the improvement is reduced but still significant and remains for the first 40mm. When compared to the two coils placed 5mm away from the phantom there is still large improvement near the surface of the phantom, however, the penetration is reduced to a depth of 20mm. It can also be seen that there is little difference between the 120mm and 150mm coil cases and as such the 150mm coil will not be studied further in this work. Fig. 4b and Fig. 4d illustrate the effect of the FSS periodicity which gives rise to localised nulls. The impact of this will be to reduce the usable field of view (FoV) in MRI acquisition, however, for applications where small anatomic features are of importance this is not a significant issue.

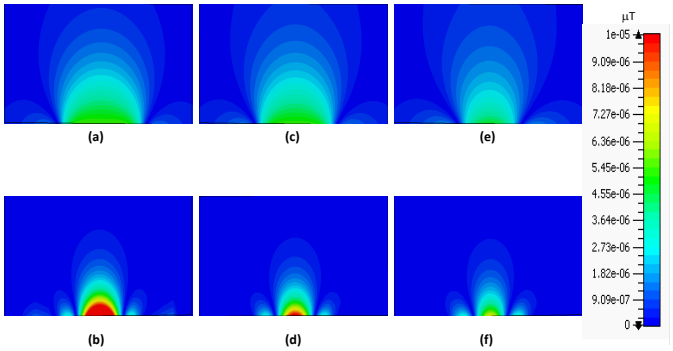

Fig. 5: Simulated $|B_1^+|$ across xy plane, (a) without CIS, (b) with CIS (z=0), (c) without CIS, (d) with CIS (z=P/2), (e) without CIS and (f) with CIS (z=P)

Further detail relating to the variation of B_1^+ for different positions across the FSS is depicted in Fig. 5 which shows the performance with and without CIS across the xy plane which includes the centre of the structure (z=0), intercell region (z=P/2) and adjacent cell centre (z=P) where localised improvement is observed for all xy slices. Nulls occur approximately at the intercell position for the case with the CIS. Only B_1^+ results are shown for brevity as similar results are observed for $|B_1^-|/\sqrt{P_{abs}}$.

For clinical MR the use of multiple 2D slices or 3D volu-

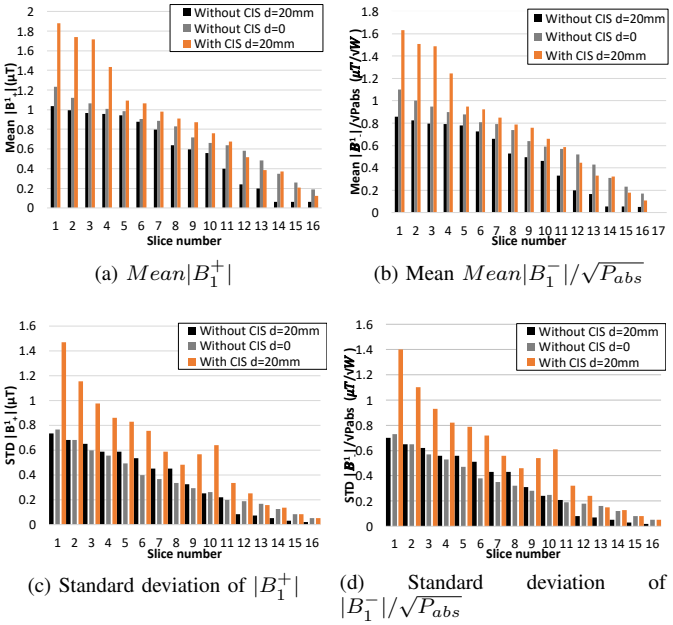

(a) $Mean|B_1^+|$ (b) Mean $Mean|B_1^-|/\sqrt{P_{abs}}$

(c) Standard deviation of $|B_1^+|$ (d) Standard deviation of $|B_1^-|/\sqrt{P_{abs}}$

Fig. 6: Simulated mean and standard deviation for varying slices of volume $(D_c/\sqrt{2} \times D_c \times 10mm)$

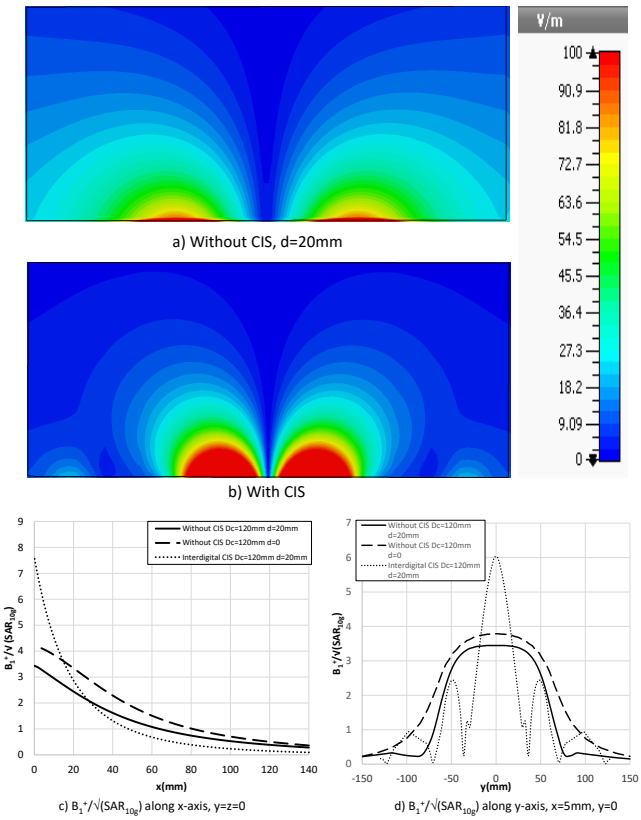

Fig. 7: Simulated E-field across xy plane, (a) without CIS (d=20mm), (b) with CIS (z=0). Simulated $\frac{B_1^+}{max(\sqrt{SAR_{10g}})}$, (c) along x-axis (x=y=0), (d) along y-axis (x=5mm, y=0)

metric acquisition is commonly used for volumetric imaging, as such simulations were carried out for a number of slices across the dielectric phantom beginning at the coil center and extending towards the phantom edge. To quantify the performance for an individual slice the mean and standard deviation of $|B_1|$ over a volume defined by $(D_c/\sqrt{2} \times D_c \times 10mm)$, where D_c is the RF coil diameter, was adopted. Due to the field symmetry only half of the phantom volume was considered. The results are shown in Fig. 6 and demonstrate up to 2-fold improvement in the mean B_1 for the first four slices and there is reasonable improvement beyond the coil edge. The power absorbed in the whole phantom is reduced by 11% when the CIS is present, which is due to a reduced electric field exposure in the phantom as a result of the field focusing, see Fig 7. The standard deviation is large for the CIS case which is due to the significant local increase in field near the surface of the phantom and also due to the field nulls.

Fig. 7a and Fig. 7b show the simulated electric fields through a cross section inside the dielectric phantom (z=0mm) for the with and without (d=20mm) CIS cases. Due to field focusing it can be seen that the CIS produces higher fields local to the phantom surface and a maximum 1.7 fold increase in field is observed. The impact of this on the specific absorption rate (SAR) on a human body model is subject to further study and is beyond the scope of this work. Fig. 7c and Fig. 7d show $\frac{B_1^+}{max(\sqrt{SAR_{10g}})}$, where $max(\sqrt{SAR_{10g}}$ is the maximum 10g specific absorption rate (SAR) within the dielectric phantom, along the x-axis (y=z=0) and y-axis (x=5mm y=0) respectively.

IV. Experimental Characterization

This section describes the electromagnetic characterization of a prototype CIS based transceiver system as a proof of concept demonstration and a comparison of performance against the RF coil alone is presented.

A. Prototype manufacture and RF characterization

The RF coil design is based on a previously reported method [15], with the coil matched to a 50Ω source. The FSS was manufactured on double sided FR4 using a PCB etching technique to the dimensions specified in Section II-B. The dielectric phantom used in the characterization comprised of a 5L solution of distilled water and approximately 20g of NaCl and 10g of CuSO4 using a thin plastic container with the same dimensions used in the simulations. A prototype RF coil was manufactured using a standard PCB etching technique and was tuned to 63.8MHz, when spaced 25mm away from a dielectric phantom and FSS, using three lumped capacitors spaced equally around the coil circumference. A further lumped capacitor was used to match the coil impedance to 50Ω. The tuning capacitance chosen was $C_1 = 68pF, C_2 = 100pF$ and $C_3 = 56pF$ when the CIS is not present with a

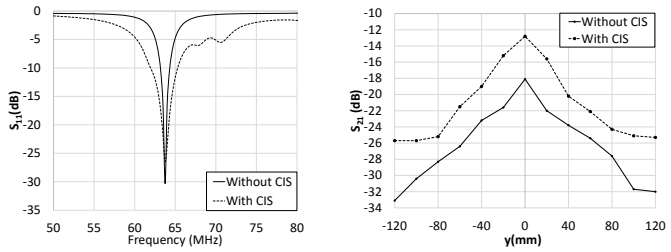

(a) S_{11}

(b) S_{21} across surface of dielectic phantom

Fig. 8: Measured S-parameters results

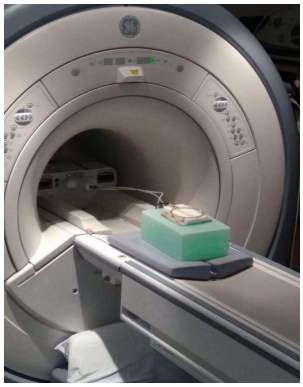

Fig. 9: 1.5T MRI scanner with CIS transceiver and dielectric phantom

matching capacitance $C_m = 168pF$ and when the CIS was present the tuning capacitance was $C_1 = 221pF, C_2 = 200pF$ and $C_3 = 68pF$ with a matching capacitance $C_m = 100pF$. It should be noted that the tuning capacitors do not need to be equal and are combinations of preferred manufacturers values. Tuning and matching was carried out using a one-port calibrated Keysight E5071B vector network analyzer (VNA) and a minimum of 25dB return loss was achieved for both with and without CIS, Fig.8a.

To characterize the magnetic field a second coil of diameter 3cm, which is chosen to have minimal influence on the magnetic field, was connected to port two of the VNA and it is assumed that the measured transmission coefficient (S_{21}) is proportional in the magnetic field [29]. Measurements were taken every 20mm, and the improvement is approximately 5dB and 7dB at the center and edges of the phantom respectively, as shown in Fig. 8b.

The loaded and unloaded Q-factor of the RF coils with and without CIS were measured and the ratio of the unloaded to loaded Q-factors were 3.06 and 3.2 respectively.

B. MRI Measurements

Axial MR images of the dielectric phantom, used in Section IV-A, were acquired on a 1.5T MRI scanner (GE HDx Milwaukee, USA) using a multi-slice 2D spoiled gradient echo pulse sequence. Three sets of image data were acquired with and without CIS (d=0 and 20mm), a photograph of the system is shown in Fig. 9 and the measurement parameters are listed in Table I.

TABLE I: MRI scanner settings

Parameter	Value
Pulse repetition time (ms)	500
Echo time (ms)	50
Bandwidth (kHz)	15.63
Field of view (cm)	36 x 36
Slice thickness (mm)	10
Acquisition matrix (pixels)	128 x 128

The signal intensity of the n^{th} pixel, *S(n)*, was analyzed to calculate the image SNR using (7),

$$SNR_n = \frac{S(n)}{\sqrt{2}\sigma_s}, \tag{7}$$

where σ_s is the standard deviation of the background noise [30].

Initially, a constant transmission power of approximately 80W was used and the SNR image is shown in Fig. 10 for the central slice. The coordinate system referred to in Fig. 10 is illustrated in Fig. 1a. Analysis of the data shows that the maximum improvement along the coil axis (x-axis) is approximately 415% and 160% when x=5mm, comparing against the d=20mm and d=0mm cases respectively. The penetration depth, compared against these two cases, are 50mm and 30mm, and thereafter the SNR remains similar to the coil only, see Fig 11a. Performance laterally across the phantom (y-axis) is shown in Fig. 11b where SNR improvement can be observed over a 200mm and 150mm width of the phantom when compared against the d=20mm and d=0mm coil only cases respectively.

Data analysis of the mean SNR from eight slice acquisitions over a $(D_c/\sqrt{2} \times D_c \times 10mm)$ volume is shown in Fig. 12 and significant improvement is observed for the first two slices (102% and 80% respectively), compared against the d=20mm case and there is an improvement of 75% and 66% for the first two slices compared against the coil only when d=0mm. The remaining slices also show improvements although reduced due to field focusing.

V. Measured transmission efficiency and receiver sensitivity

A. Transmission efficiency

To quantify the RF coil transmission efficiency a range of images were acquired for varying transmit power to determine the flip angle at each pixel. To achieve this a curve fitting algorithm was implemented to map the measured SNR to (1), provide earlier. It was assumed that the transmit power was delivered to a 50Ω transceiver and that the $|B_1^+|$ is proportional to the transmit voltage. As an example of the curve fitting algorithm the normalized SNR against RMS voltage is shown in Fig. 13 for a pixel close to the surface of the dielectric phantom where the SNR is normalized to the maximum fitted value when the CIS is present. It can be seen that the maximum SNR of the RF coil alone occurs at approximately 200V

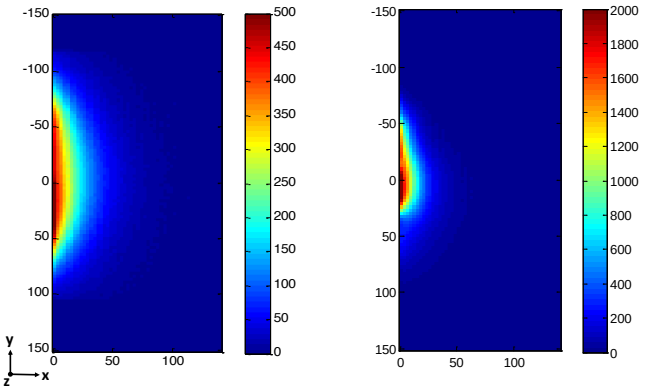

(a) without CIS, d=20mm (b) with CIS

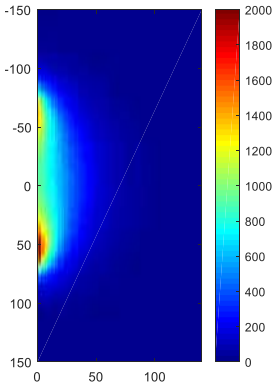

(c) without CIS, d=0mm

Fig. 10: Measured SNR at the coil center (z=0). Transmit power of 80W

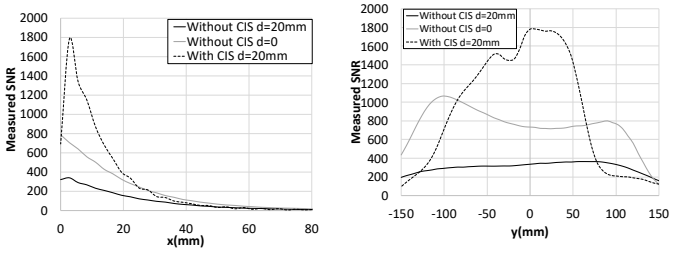

(a) SNR along x-axis (y=0, z=0) (b) SNR along y-axis (x=5, z=0)

Fig. 11: Measured SNR. Transmit power of 80W

and 125V, for the d=20mm and d=0mm cases respectively, compared to 66V when the CIS is present translating to a maximum of 3 fold reduction in voltage or a 9 fold reduction in transmit power to achieve the same $|B_1^+|$. The difference in magnitude translates to improvement in $|B_1^-|$ where a 2.4 and 1.6 fold improvement can also be observed, for the d=20mm and d=0mm cases respectively. Using this approach, the flip angle at each pixel can be estimated and an example of this,

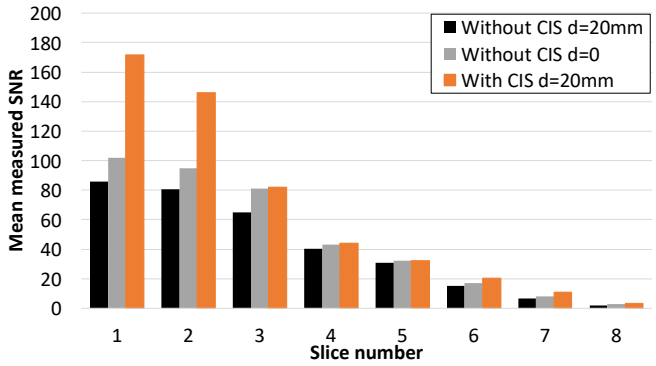

Fig. 12: Mean measured SNR for varying slices of volume $(D_c/\sqrt{2}\times D_c \times 10mm)$. Transmit power of 80W.

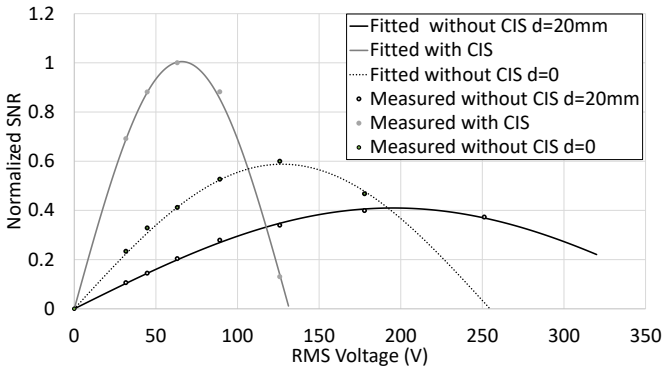

Fig. 13: Measured and curved fitted SNR versus transmit RMS voltage for a single voxel near the phantom surface

for a transmit power of 80W, is shown in Fig. 14 (Note that only pixels where the SNR was greater than 10 times the background noise were used to reduce errors in the curve fitting algorithm). The results show a region of high flip angle when the CIS is present with a maximum improvement of 216% and improvement can be seen for a penetration depth of 40mm, when d=20mm. For the d=0mm case there is still flip angle improvement near the surface of the phantom, however, the penetration depth is reduced. Finally, the mean pixel flip angle averaged over a volume $D_c/\sqrt{2}\times D_c \times 10mm$, was calculated for all transmit powers and is shown in Table II where the values are given to the nearest degree due to the uncertainties associated with flip angle homogeneity. Data for the center slice (z=0), intercell slice (z=P/2) and adjacent slice (z=P) are provided when d=20mm for the coil only case. It can be seen that for all transmit powers the mean slice flip angle is higher when the CIS is present.

B. *Receiver sensitivity*

To make a fair comparison of receiver sensitivity the effect of transmit efficiency needs to be taken into account. To achieve this the SNR is normalised by the sine of the flip

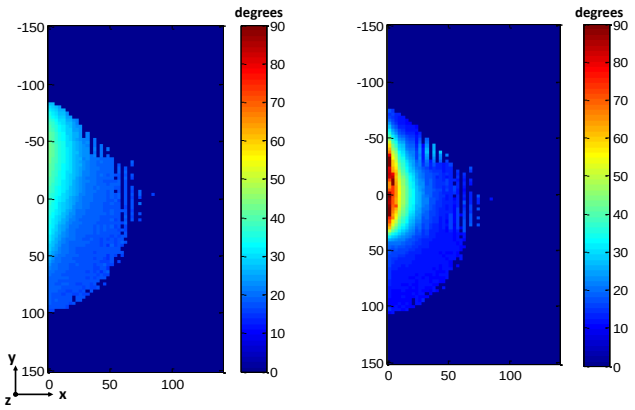

(a) Without CIS (d=20mm), α_{coil} (b) With CIS, α_{CIS}

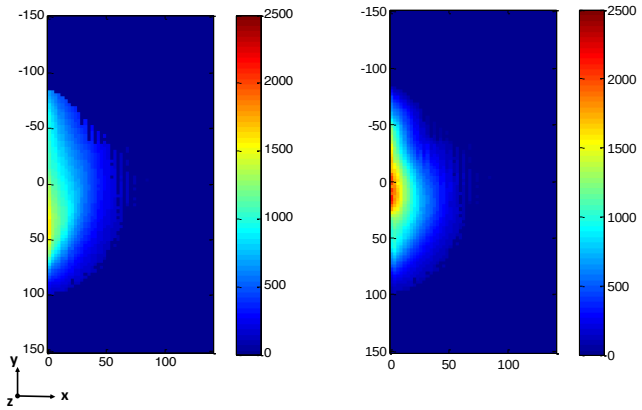

(a) Without CIS (d=20mm), Ψ_{coil} (b) With CIS, Ψ_{CIS}

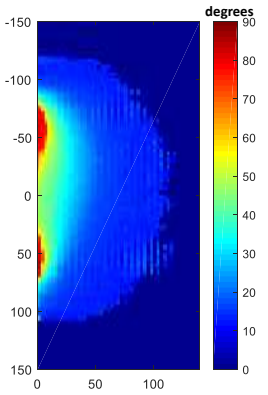

(c) Without CIS (d=0mm), α_{coil}

Fig. 14: Measured flip angle map for transmit power of 80W

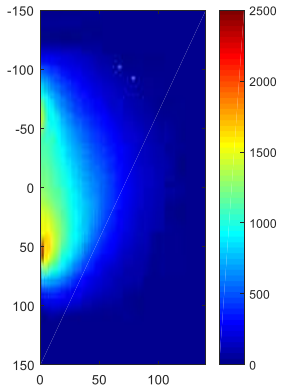

(c) Without CIS (d=0mm), Ψ_{coil}

Fig. 15: Measured receiver sensitivity for a transmit power of 80W.

TABLE II: Measured mean slice flip angle, (°). Note that the without CIS data is when d=20mm.

	Centre slice		Intercell slice		Adjacent slice	
Power (W)	αg_{coil}	αg_{CIS}	αg_{coil}	αg_{CIS}	αg_{coil}	αg_{CIS}
20	10	17	9	12	7	8
40	15	20	12	14	9	11
80	24	30	15	19	15	17
159	28	34	22	26	18	24
317	31	49	29	34	22	26
632	38	56	37	42	29	40
1262	52	66	50	62	35	52

TABLE III: A comparison between CIS method against the state-of-art 1.5T methods from published literature. Note: * denotes a lens method, all others are metasurface

Ref	SNR Increase (%)	Penetration (mm)	Dimensions (mm)
[10]*	100	35	270x270x30
[17]	170	70	255x154x22
[18]	170	40	175x175x9
[21]	500	140	130x380x198
[22]	140	60	414x200x73
[This paper]	415	50	150x150x0.8

angle at each xy pixel as defined in (8) and (9),

$$\Psi_{CIS}(x,y) = \frac{SNR_{CIS}(x,y)}{sin(\alpha_{CIS}(x,y))} \tag{8}$$

$$\Psi_{coil}(x,y) = \frac{SNR_{coil}(x,y)}{sin\left(\alpha_{coil}(x,y)\left(\frac{\alpha g_{CIS}}{\alpha g_{coil}}\right)\right)}, \tag{9}$$

where SNR_{coil} and SNR_{CIS} are the SNR without and with CIS respectively. Likewise, α_{coil} and α_{CIS} are the flip angle without and with CIS respectively. It was previously shown that the with/without CIS mean slice flip angle is not the same for a given transmit power, hence for a fair comparison $\alpha_{coil}(x,y)$ is modified by the mean slice flip angle ratio of the two cases $\left(\frac{\alpha g_{CIS}}{\alpha g_{coil}}\right)$. Fig. 15 shows the receiver sensitivity for a transmit power of 80W for the CIS and without CIS (d=0mm and d=20mm) cases. A maximum improvement, when compared against without CIS (d=20mm), of 133% can be achieved and useful improvements can be seen over the majority of the region of interest.

VI. Conclusion

A method for designing a capacitive impedance surface for enhancing surface coil performance for MRI applications at 1.5T has been demonstrated where it has been shown to locally improve performance close to the surface of a dielectric phantom. Numerical simulations have shown the potential to achieve maximum $|B_1^+|$ and $|B_1^-|/\sqrt{P_{abs}}$ localized improvements of 200% and 160% respectively, when compared with no CIS. Experimental results show a 5dB increase in transmission efficiency at the coil centre when tested within a two port VNA system at the front face of a dielectric phantom. MRI measurements using a 1.5T scanner have shown similar trends giving a maximum improvement of 216%, 133%, and 415% for transmission efficiency, receiver sensitivity, and SNR improvement for a particular transmission power respectively. Multiple slice acquisition results show improvement for all the slices when CIS is compared to coil alone. Table III shows a comparison between using the proposed CIS method with the state-of-art showing how the compact nature of our design is advantageous. This approach could be useful for close-to-surface high resolution feature imaging, for example extremities and breast imaging, where the required depth of penetration is a few centimeters. The approach may also be beneficial for reducing the required RF power for a particular flip angle. Future work will focus on array implementation and multi-resonant (multi-nuclear) designs for hyper polarized gas lung imaging applications.

Acknowledgements

We would like to acknowledge Mr Tingzhao Yang and Mr Adam Maunder for their assistance in coil manufacture and carrying out MRI measurements.

References

[1] J. T. Vaughan and J. R. Griffiths, *RF Coils for MRI*. Wiley, 2012.

[2] M. Brown and R. Semelka, *MRI: Basic Principles and Applications*. Wiley, 2003.

[3] K. Ugurbil, "Magnetic resonance imaging at ultrahigh fields," *IEEE Transactions on Biomedical Engineering*, vol. 61, no. 5, pp. 1364–1379, 2014.

[4] N. Engheta and R. Ziolkowski, *Metamaterials: Physics and Engineering Explorations*. John Wiley & Sons, Inc., 9 2006.

[5] S. B. Glybovski, S. A. Tretyakov, P. A. Belov, Y. S. Kivshar, and C. R. Simovski, "Metasurfaces: From microwaves to visible," *Physics Reports*, vol. 634, pp. 1 – 72, 2016, metasurfaces: From microwaves to visible. [Online]. Available: http://www.sciencedirect.com/science/article/pii/S0370157316300618

[6] Q. Yang, S. Rupprecht, W. Luo, C. Sica, Z. Herse, J. Wang, Z. Cao, J. Vesek, M. Lanagan, G. Carluccio, Y.-C. Ryu, and C. Collins, "Radiofrequency field enhancement with high dielectric constant (hdc) pads in a receive array coil at 3.0t," *Journal of Magnetic Resonance Imaging*, vol. 38, no. 2, pp. 435–440, 2013, cited By 25.

[7] M. Wiltshire, J. Pendry, I. Young, D. Larkman, D. Gilderdale, and J. Hajnal, "Microstructured magnetic materials for RF flux guides in magnetic resonance imaging," *Science*, vol. 291, no. 5505, pp. 849–851, 2001.

[8] M. J. Freire, R. Marques, and L. Jelinek, "Experimental demonstration of a μ=- 1 metamaterial lens for magnetic resonance imaging," *Applied Physics Letters*, vol. 93, no. 23, 2008.

[9] J. Algarin, M. Lopez, M. Freire, and R. Marques, "Signal to noise ratio evaluation in resonant ring metamaterial lenses for MRI applications," *New Journal of Physics*, vol. 13, no. 11, 2011.

[10] J. M. Algarín, M. J. Freire, F. Breuer, and V. C. Behr, "Metamaterial magnetoinductive lens performance as a function of field strength," *Journal of Magnetic Resonance*, vol. 247, pp. 9–14, 2014.

[11] G. Saleh, K. Solbach, and A. Rennings, "EBG structure to improve the B1 efficiency of stripline coil for 7 Tesla MRI," in *Proceedings of 6th European Conference on Antennas and Propagation, EuCAP 2012*, 2012, pp. 1399–1401.

[12] Z. Chen, K. Solbach, D. Erni, and A. Rennings, "Improved B1 distribution of an MRI RF coil element using a high-impedance-surface shield," in *2015 German Microwave Conference*, March 2015, pp. 111–114.

[13] ——, "Improving B1 efficiency and signal-to-noise-ratio of a surface coil by a high-impedance-surface RF shield for 7-T magnetic resonance imaging," *IEEE Transactions on Microwave Theory and Techniques*, vol. 65, no. 3, pp. 988–997, 2017.

[14] I. M. Issa, L. K. Ford, J. M. Wild, and M. Rao, "A high impedance surface for improving the radio frequency magnetic field for a 1.5 Tesla magnetic resonance system," in *2015 Loughborough Antennas Propagation Conference (LAPC)*, Nov 2015, pp. 1–4.

[15] I. Issa, K. L. Ford, M. Rao, and J. Wild, "Enhancement of radio frequency magnetic field for a 1.5 T magnetic resonance system using a high impedance surface," *IET Microwaves, Antennas Propagation*, vol. 10, no. 13, pp. 1378–1383, 2016.

[16] X. Radu, D. Garray, and C. Craeye, "Toward a wire medium endoscope for mri imaging," *Metamaterials*, vol. 3, no. 2, pp. 90 – 99, 2009.

[17] A. P. Slobozhanyuk, A. N. Poddubny, A. J. Raaijmakers, C. A. van den Berg, A. V. Kozachenko, I. A. Dubrovina, I. V. Melchakova, Y. S. Kivshar, and P. A. Belov, "Enhancement of magnetic resonance imaging with metasurfaces," *Advanced Materials*, 2016.

[18] R. Schmidt, A. Slobozhanyuk, P. Belov, and A. Webb, "Flexible and compact hybrid metasurfaces for enhanced ultra high field in vivo magnetic resonance imaging," *Scientific reports*, vol. 7, no. 1, p. 1678, 2017.

[19] A. V. Shchelokova, C. A. van den Berg, D. A. Dobrykh, S. B. Glybovski, M. A. Zubkov, E. A. Brui, D. S. Dmitriev, A. V. Kozachenko, A. Y. Efimtcev, A. V. Sokolov, V. A. Fokin, I. V. Melchakova, and P. A. Belov, "Volumetric wireless coil based on periodically coupled split-loop resonators for clinical wrist imaging," *Magnetic Resonance in Medicine*, vol. 80, no. 4, pp. 1726–1737, 2018.

[20] E. A. Brui, A. V. Shchelokova, M. Zubkov, I. V. Melchakova, S. B. Glybovski, and A. P. Slobozhanyuk, "Adjustable subwavelength metasurface-inspired resonator for magnetic resonance imaging," *physica status solidi (a)*, vol. 215, no. 5, pp. 1–6, 2018.

[21] A. V. Shchelokova, A. P. Slobozhanyuk, I. V. Melchakova, S. B. Glybovski, A. G. Webb, Y. S. Kivshar, and P. A. Belov, "Locally enhanced image quality with tunable hybrid metasurfaces," *Phys. Rev. Applied*, vol. 9, p. 014020, Jan 2018.

[22] E. I. Kretov, A. V. Shchelokova, and A. P. Slobozhanyuk, "Impact of wire metasurface eigenmode on the sensitivity enhancement of mri system," *Applied Physics Letters*, vol. 112, no. 3, p. 033501, 2018.

[23] D. Hoult, "The principle of reciprocity in signal strength calculationsa mathematical guide," *Concepts in Magnetic Resonance Part A*, vol. 12, no. 4, pp. 173–187, 2000.

[24] C. M. Collins and M. B. Smith, "Signal-to-noise ratio and absorbed power as functions of main magnetic field strength, and definition of 90 RF pulse for the head in the birdcage coil," *Magnetic Resonance in Medicine*, vol. 45, no. 4, pp. 684–691, 2001.

[25] I. Issa, K. L. Ford, M. Rao, and J. Wild, "Evaluation of high impedance surfaces for MRI RF coil applications-simulations of RF field and specific absorption rate," in *Antennas and Propagation (EuCAP), 2016 10th European Conference on*. IEEE, 2016, pp. 1–3.

[26] K. R. Foster and H. P. Schwan, "Dielectric properties of tissues and

biological materials: a critical review." *Critical Reviews in Biomedical Engineering*, vol. 17, no. 1, pp. 25–104, 1989.

[27] M. Stuchly and S. Stuchly, "Dielectric properties of biological substances-tabulated," *Journal of Microwave Power*, vol. 15, pp. 19–26, 1980.

[28] I. J. Bahl, *Lumped Elements for RF and Microwave Circuits*. Artech House, 2003.

[29] D. M. Pozar, "Microwave engineering 3rd ed., MA John Wiley & Sons," 2005.

[30] O. Dietrich, J. G. Raya, S. B. Reeder, M. F. Reiser, and S. O. Schoenberg, "Measurement of signal-to-noise ratios in MR images: Influence of multichannel coils, parallel imaging, and reconstruction filters," *Journal of Magnetic Resonance Imaging*, vol. 26, no. 2, pp. 375–385, 2007.